Journal of Geomatics Vol 12 No. 1 April 2018

Evaluation of the performance of the fused product of Hyperion and RapidEye red edge bands in the context of classification accuracy

Ritu Anilkumar, Dibyajyoti Chutia, Jonali Goswami, Vikas Sharma and PLN Raju
North Eastern Space Applications Centre, Department of Space, Government of India
Umiam, Shillong, Meghalaya, India- 793103
Email: ritu.anilkumar@nesac.gov.in, d.chutia@nesac.gov.in,
jonali.goswami@gmail.com, vikashsharmamy@gmail.com, raju@nesac.gov.in

(Received: Feb 07, 2018; final form: Apr 16, 2018)

Abstract: Satellite images are characterized by a large number of features in spectral and spatial domain. However, due to SNR constraints, development of a high spatial resolution and spectral resolution sensor is challenging. Hence, fusion techniques were developed for incorporating the spatial characteristics from a high spatial resolution multispectral or panchromatic sensor and the spectral information from the hyperspectral sensor of low spatial resolution. Here, the fusion was achieved by utilizing the Gram-Schmidt orthogonalization procedure and classification was performed on the obtained high spatial and spectral resolution image and a case study over the Dhemaji and Lakhimpur districts of Assam, India was performed. Investigations were carried out utilizing the Hyperion image, RapidEye image, fused image and the Red Edge subsets of the Hyperion and fused data sets where a number of vegetation, water and land cover classes have been selected for three test sites. All comparisons were performed using standard supervised classifiers such as maximum likelihood classifier, spectral angle mapper and support vector machines with the polynomial and radial basis function kernel. RapidEye data classifies the scene best with the MLC classifier. SVM classifiers with RBF or polynomial kernels perform consistently better with Hyperion and fused data sets. Red Edge subsets of the Hyperion and fused images are observed to perform well with both MLC and SVM classifiers.

Keywords: Hyperspectral remote sensing, Hyperion, Fusion, Classification, Red Edge, Spectral sharpening

1. Introduction

The economy of India is primarily agrarian with 56.3% of its population dependent upon agriculture as a source of income and 17.32% contribution to the GDP (Ministry of Statistics and Programme Implementation). Modern agriculture has seen rapid improvements starting with mechanization during the industrial revolution to manipulation of the genetic structure of the crop. Technological advancements in the form of accurate navigation systems and sophisticated satellite and airborne sensors have permitted large scale monitoring of agricultural structures. Over the last decade, space based instruments such as RapidEye, QuickBird, LandSat, CartoSat, Hyperion, Compact High Resolution Imaging Spectrometer/Proba (CHRIS/Proba) etc have gained much importance in precision agriculture. This is particularly reflected in the introduction of the Red Edge band in the sensors. Red Edge refers to the sharp increase in reflectance as observed in the vegetation spectrum beyond the red wavelengths, generally from 680-750 nm (Vogelmann, 1993, Penuelas et. al., 1995, Cho et. al., 2008). Horler et. al. 1983, Dawson and Curran, 1998 and Schulster et. al., 2012 document two reasons for this prominent Red Edge in vegetation: (1) strong chlorophyll absorption in the red region of the electromagnetic spectrum and (2) high internal leaf scattering causing a strong reflectance of the near infrared region of the electromagnetic spectrum.

1.1 Classical techniques and challenges

Early studies in crop stage discrimination, plant health monitoring or even species identification using the Red Edge region were established (Gupta et. al. 2003, Smith et. al. 2004). However, the large weight of the instruments and costs associated with such techniques led to the necessity of using broad band, multispectral sensors for the same. Plenty of studies have performed classification of multispectral images utilizing spectral indices generated out of manipulating the features of the spectrum (Jackson and Huete, 1991, Schuster et. al., 2012, Ustuner et. al. 2015). However, these methods face a significant drawback as a result of the broad band nature of multispectral imaging being unable to map the finer aspects of the spectrum (Ferrato and Forsythe, 2012). To cater to this specific advantage, hyperspectral imaging sensors for space borne and airborne applications were developed and improved significantly over the last two decades (Pignatti et. al., 2009; Purkis and Klemas, 2011; Heiden et. al., 2012). Through hyperspectral imagery, we are now able to monitor crop health utilizing the chlorophyll and photosynthesis related absorptions at 437 (chlorophyll a), 460 (chlorophyll b), 642 (chlorophyll a) and 659 nm (chlorophyll b) (Porra et. al., 1989, Penuelas et. al., 1995, Wu et. al., 2008), 705 nm (chlorophyll absorption Wu et. al., 2008), 530, 735 nm (indicating photosynthesis Lang et. al., 1991). Soil moisture studies can be performed to optimize growth parameters possible in VNIR as well as SWIR due to soil-water interactions from 350 nm to 2500 nm (Gao, 1996, Ceccato et. al., 2001, Champagne et. al., 2003, Stimson et. al., 2005). Vegetation parameters such as Leaf Area Index, biomass are estimated using the Red Edge specifically from 680 to 750 nm (Vogelmann, 1993, Penuelas et. al., 1995, Cho et. al., 2008). Plant physiological parameters including nitrogen content using 1510, 1680 nm bands (Penuelas et. al. 1995, Serrano et. al., 2002), lignin using 1680 and 1754 nm bands and cellulose quantification using bands from 2000

to 2200 nm (Serrano et. al., 2002, Daughtry et. al. 2006) can be achieved. Moisture related plant stress can also be studied due to the water absorptions at 1400 and 1900 nm (Gao 1996, Ceccato et. al. 2001).

1.2 Motivation and contributions

Hyperspectral imagery permits a precise measurement of the radiant flux (Jensen and Im, 2007) and the differentiation of a variety of agricultural species and crop health stages. They however fail spatially due to the trade-off between spectral resolution, spatial resolution and Signal to Noise Ratio (SNR) (Yokoya et. al., 2017). This inherent trade-off between spatial resolution, spectral resolution and SNR prompted the necessity to use image processing techniques to use the spatial information of high resolution panchromatic imagery and spectral information from hyperspectral imagery thereby metaphorically being able live in the best of both worlds. This process is called fusion. The fused data sets along with hyperspectral and multispectral data sets were compared for their classification accuracy using standard classifiers such as support vector machines (SVM), spectral angle mapper (SAM) and maximum likelihood classifier (MLC). The major contributions of this study are summarized as follows:

1. Performing fusion of Hyperion data set with the Red Edge band of the RapidEye data set via the technique of Gram Schmidt spectral sharpening to yield a high spatial and spectral resolution image.

2. Classification of the multispectral image, hyperspectral image and fused image using SVM (using radial basis function (RBF) kernel and polynomial kernel of order 3), SAM and MLC to evaluate the utility of the fused product.

2. Data used and study area

This study attempts to characterize vegetation by emphasising on the Red Edge bands of Hyperion data and compare classification results of hyperspectral imagery from Hyperion, multispectral imagery from RapidEye and a fused product of the same. Characteristics of the Hyperion and RapidEye sensors are tabulated in table 1.

2.1 Satellite imagery used

Earth Observer-1 Hyperion: Hyperion (Pearlmann, et al., 2003) is a hyperspectral sensor on board the NASA (National Aeronautics and Space Administration) Earth Observer 1 (EO-1) which functioned from November, 2001 to April, 2016. With a 242 channels ranging from the VNIR (Visible and Near Infrared) to SWIR (Short Wave Infrared), 400 to 2500 nm, Hyperion images at a spatial resolution of 30m and a radiometric resolution of 12bits. Hyperion data is available as level 1, radiometrically calibrated product (Level 1R) as well as geometrically corrected and georeferenced data (Level1 GST and IT) at the USGS (United States Geological Survey) website Earth Explorer: https://earthexlorer.usgs.gov. Each of these datasets need to be further corrected before they can be used to develop products of our interest. Of the 242 bands, some are highly noisy and a redundancy exists due to the overlap of detecting regions by the VNIR and SWIR detector. Hence we ignore these bands and the total usable bands comes down to 196 (1-7, 58-78 and 225-242 are removed). This is followed by correction due to effects of the atmosphere. The corrections often reduce the SNR. To correct for this, attempts to separate the noise from the data are performed using the Minimum Noise Fraction (MNF) denoising technique (Green et. al., 1998).

RapidEye: The RapidEye constellation is a set of 5 satellites designed and developed by Surrey Satellite Technology Ltd in 2008 and later acquired by Planet in 2015. It provides imagery of 5m/pixel spatial resolution in 5 bands (red, green, blue, red-edge and near infrared) available at the Planet Server webpage. With an elevation of 630km and a 77km swath, RapidEye has a revisit time of 5.5 days at nadir. All five satellite sensors are calibrated similarly leaving no distinction between satellite imagery from any sensor. The mosaic of 5 level 3 ortho-corrected imagery was used for this study. Atmospheric correction was performed using the Quick Atmospheric Correction (QuAC) technique. (Bernstein et al., 2005).

2.2 Study area

The study area is the Dhemaji and Lakhimpur region of Assam which is abundant in rice crop cultivation. Hence, the Red Edge region is specifically used for further discrimination within the vegetation class. Dhemaji district of Assam is bounded by Arunachal Pradesh in the North and the river Brahmaputra in the South. It is a plain area with an average elevation of 104 m above sea level. Numerous drainage systems originating from the hills of Arunachal Pradesh flow through Dhemaji to drain into the Brahmaputra. Physiographically, Dhemaji is in the form of three main sub districts: the piedmont zone where Dhemaji borders the Arunachal Himalayas, the active flood plains near the river Brahmaputra and its tributaries, and the low lying alluvial belt.

Table 1: Sensor information for the Hyperion and RapidEye instruments

Instrument/ Parameter	Wavelength Range nm	No of spectral channels	Spectral Resolution	Spatial Resolution	Quantization
EO-1/Hyperion	400-2500	242	10nm (detector dependant)	30m	12 bits
RapidEye	440-850	5	non-uniform	5m	12 bits

With a total geographic area of 323,700 ha. Dhemaji covers a variety of socio-geographic features including build up (208 ha), horticultural lands (2534 ha), forest cover (53,225 ha) and grasslands (97,167 ha), making it a perfect study area for the classification techniques aimed towards vegetation. Three Test Sites were selected across Dhemaji and Lakhimpur and data of Hyperion and RapidEye taken on October, 2012 were analysed and regions of interest were selected based on the existing Land Use Land Cover (LULC) map for 2011-2012. Each region and the subsequent classes we have classified into are summarized below. The Test Sites used for the study are depicted in figure 1. Details of training and test samples are available in table 2-4.

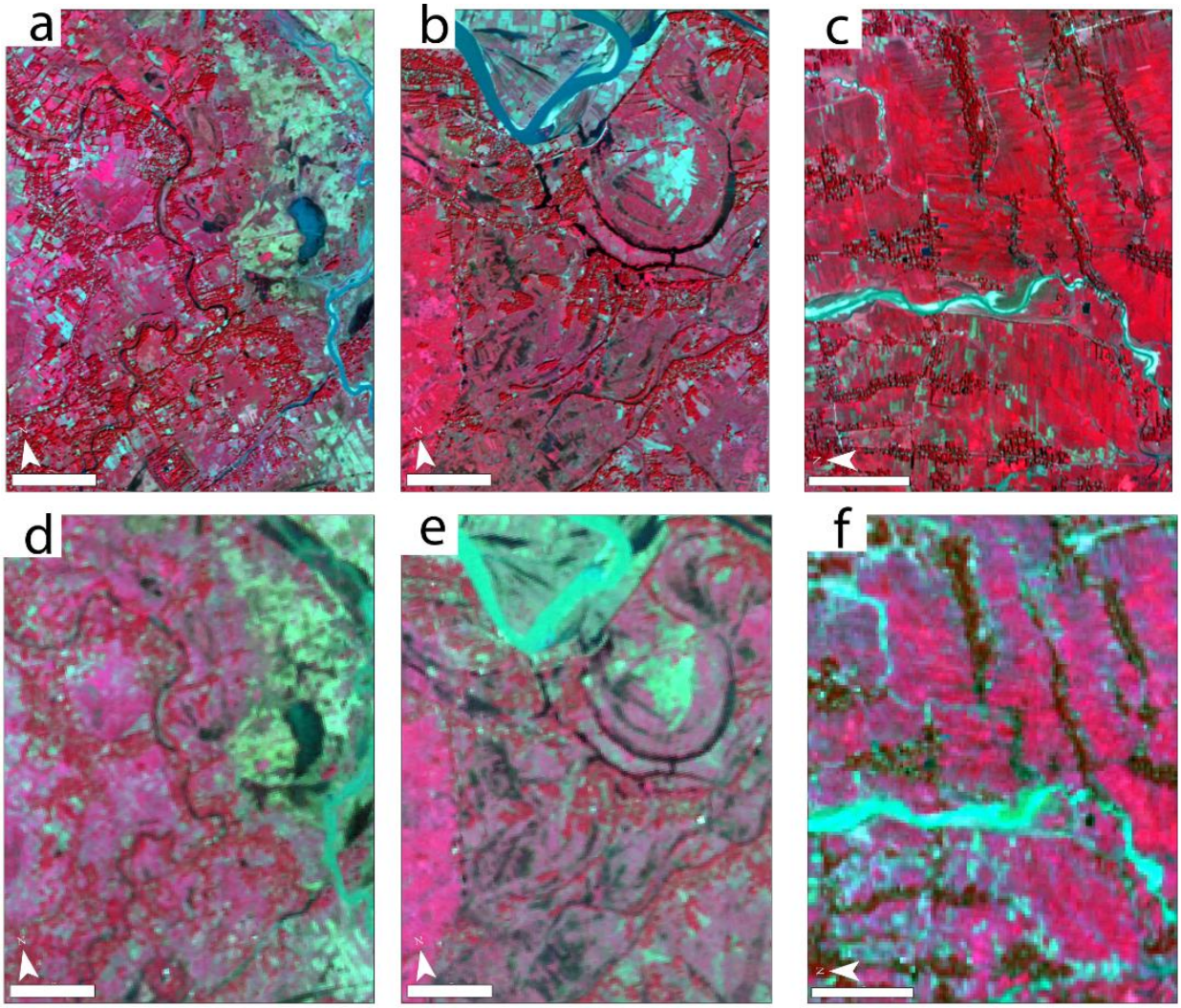

Figure 1: False colour composite (NIR, Red, Green) for Test Site 1, 2 and 3 respectively obtained using RapidEye (fig: 1a-1c, band combination: 5, 3 and 2) and Hyperion data sets (fig: 1d-1f, band combination: 44, 23 and 13)

Table 2: Information on the testing and training samples for each class of Test Site 1

S.No	Class name	Hyperion		RapidEye	
		Train Size	Test size	Train Size	Test size
1	Kharif crop	696	176	6162	4933
2	Open forest	358	156	12642	5455
3	Fallow	362	176	3322	3382
4	Water Body	293	154	4571	1576

Table 3: Information on the testing and training samples for each class of Test Site 2

S.No	Class name	Hyperion		RapidEye	
		Train Size	Test size	Train Size	Test size
1	Kharif crop	180	628	5094	5563
2	Perennial River	149	323	2704	2580
3	Inland Wetland	140	240	1742	2115
4	Fallow	162	227	2846	2407
5	Open forest	168	261	3711	3064

Table 4: Information on the testing and training samples for each class of Test Site 3

S.No	Class name	Hyperion		RapidEye	
		Train Size	Test size	Train Size	Test size
1	Open forest	223	260	1276	1330
2	Perennial River	172	190	761	1860
3	Fallow/Sandy	128	108	732	1207
4	Kharif Crop	190	262	6862	2283
5	Double Crop	119	119	4305	1516

Test Site 1: This Test Site depicts mainly the following features in the LULC map. A perennial and non-perennial drainage system, agricultural lands, fallow lands and open forests surrounding the rural build up near the water bodies. As the rural build up was evident only in the form of a few pixels in the RapidEye image, we have selected four classes for this site: (1) water body, (2) vegetation type 1 for agricultural lands of the kharif crop, (3) vegetation type 2 for dense open forest regions intermingled with rural build up and (4) fallow lands.
Test Site 2: This site is geographically similar to site one. There exists a perennial water body as well as waterlogged regions, agricultural lands, fallow lands and open forest around rural build up. Five classes were selected: (1) water body (perennial), (2) vegetation type 1 for agricultural lands (kharif), (3) vegetation type 2 for open forests, (4) fallow lands and (5) water logged inland wetlands. The similarity with site 1 was maintained so that accuracies could be checked in varying the number of classes.

Test Site 3: Five classes were selected for this site. However, a larger variety of vegetation types were selected to check if the Red Edge bands could accurately assess the class type. The classes selected are as follows: (1) water body, (2) vegetation type 1 for agricultural lands, (3) vegetation type 2 for agricultural lands, (4) open forests and (5) barren/fallow lands.

3 Methodology

A Hyperion strip over the Dhemaji and Lakhimpur districts of Assam taken on October, 2012 was used. RapidEye images over the same site for October, 2012 at similar local times were mosaicked and subsetted to the same areal extent as the Hyperion data. This was followed by georeferencing the Hyperion data set to the RapidEye data set using control points. Once both datasets were prepared, the processing in the form of bad band removal was performed for Hyperion and atmospheric corrections were performed on both Hyperion and RapidEye images. The corrected and georeferenced images were fused using the Gram-Schmidt hyperspectral sharpening method. The original Rapid Eye image, Hyperion image and fused image is displayed in figure 2 a, b and c respectively. The spectral characteristic of the region is as observed in figure 3 a, b and c. Hyperspectral datasets require significant denoising for enhanced spectral understanding. Hence, the MNF transformation as implemented by Green et. al., 1998 was used. A spectral subset of the fused image and the Hyperion image in the Red Edge region was also considered to understand if a Red Edge based classification depicts superior results in the case of vegetation classification.

3.1 Fusion

Multiple previous studies (Chutia et al, 2010, Pohl, 2013, Akhtar et. al., 2015, Yokoya et. al., 2017) have been performed using fusion of hyperspectral or multispectral images and panchromatic high resolution images. Yokoya et. al., 2017 has further performed a comparison of results for the different fusion methods for a variety of datasets including AVIRIS, HyDICE etc. Many fusion algorithms exist which vary in the accuracy either resulting in spatial or spectral distortions (Zhang et. al., 2007; Yakoya et. al., 2012; Qian and Chen, 2012). Recent years have seen more sophisticated attempts at the hyperspectral fusion challenge. Chen et.al.., 2014 performed fusion by dividing the multispectral image into individual bands and hyperspectral image into segments of bands centred around a corresponding multispectral band and performed pan sharpening on each segment. In this study, we use the Gram Schmidt spectral sharpening method (Laben and Brower, 2000; Maurer, 2013).

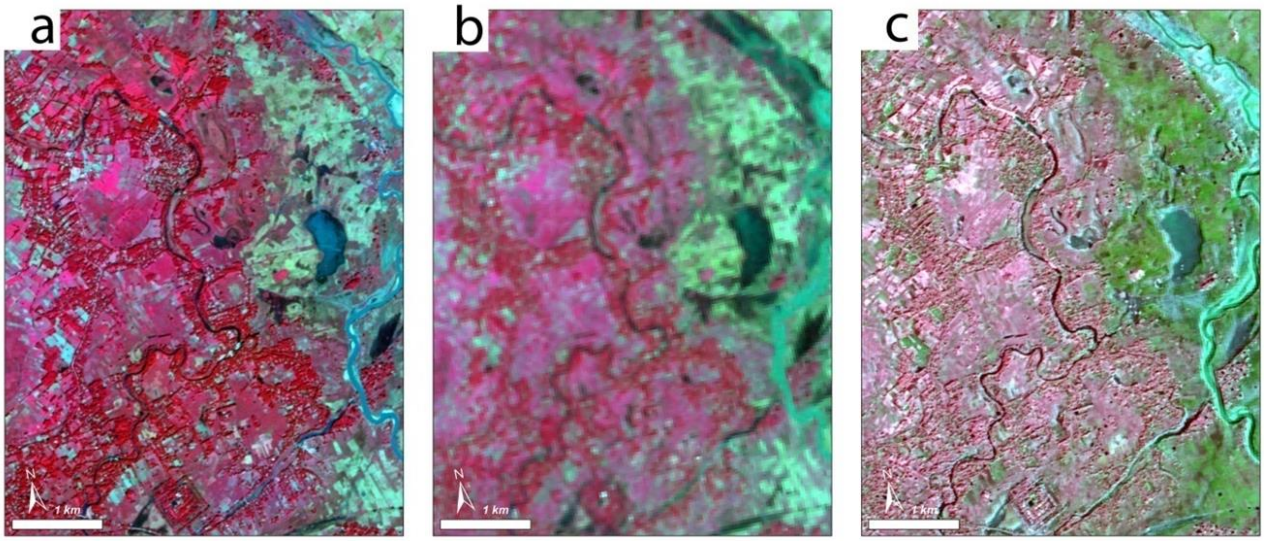

Figure 2: Spatial characteristics of the (a) RapidEye image, (b) Hyperion image and (c) Fused image as observed over Test Site 1

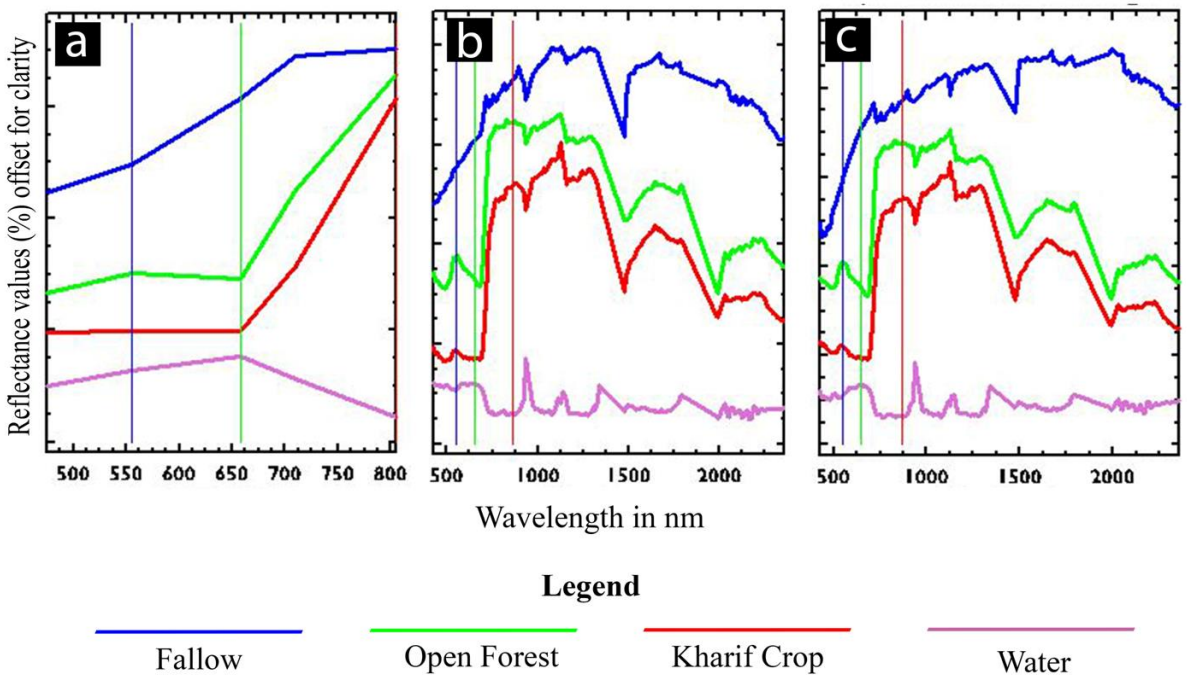

Figure 3: Spectral characteristics of the (a) RapidEye image, (b) Hyperion image and (c) Fused image as observed over Test Site 1

This involves the hyperspectral image combined via a linear combination by using weights to represent it as a panchromatic image.

$$PAN_{sim} = \sum_{i=1}^{N} w_i H_i \quad \text{... (1)}$$

This is followed by the Gram Schmidt orthonormalization of the vectors in the N dimensional space where each band represents an N dimensional vector where N is the number of pixels. This procedure decorrelates the bands. The orthonormalization procedure involves the pan band taken as the first vector (v_1). It follows the general formula as follows where u_i is the orthonormal vector and v_i is the original vector:

$$u_1 = v_1 \quad \text{... (2)}$$

$$u_i = v_i - \sum_{j=1}^{i-1} \left(\frac{u_j^T v_i}{u_j^T u_j} \right) v_i \quad \text{... (3)}$$

This is followed by replacing the averaged panchromatic image with the high spatial resolution panchromatic image and performing an inverse Gram Schmidt transform (similar to the forward transform). This gives us the fused product.

In order to check for the validity of the fused product, point to point spectral correlation was investigated between the fused data and the Hyperion data and the correlation coefficient and regression coefficient were calculated.

3.2 Classification

Three Test Sites within the Dhemaji-Lakhimpur region was considered. Classification was performed using ROIs derived from the LULC map and visual examination of the images. Hyperspectral classification techniques are adversely affected by the Houghes effect due to which the required number of training samples for larger number of bands increases to maintain the accuracy (Chutia et. al., 2015). Breunig et. al., 2011 suggest that the SVM and SAM classifiers do not demonstrate a reduction in accuracy. Hence, these two classifiers were used for the purpose. Classification was performed on the three test sites using RapidEye, Hyperion and the fused result of RapidEye and Hyperion with classes defined in accordance to the existing LULC map and the results were assessed by comparing the kappa coefficient and accuracy assessment. For a comprehensive list of hyperspectral classification techniques, refer to Chutia et. al., 2015.

3.2.1 Spectral Angle Mapper (SAM) Classifier

SAM is a classifier that compares the similarity between the test and training samples by considering the spectrum to be a D dimensional vector where D is given by the number of bands (Yuhas et. al., 1992). The training samples are either the laboratory spectra in the form of spectral libraries that have been resampled to the dimensionality of the test samples. Alternately, they are obtained from known regions within the satellite imagery that is being classified. This study uses ROIs as obtained from a ground survey performed in the Dhemaji and Lakhimpur district in 2012. Spectral similarity is estimated by calculating the angle between the test and training spectrum vectors.

$$\alpha = \cos^{-1}\left[\frac{\sum_{i=1}^{D} T_i R_i}{\left(\sum_{i=1}^{D} T_i^2\right)^{\frac{1}{2}}\left(\left(\sum_{i=1}^{D} R_i^2\right)^{\frac{1}{2}}\right)}\right] \text{---- (4)}$$

Larger angles suggest dissimilarity. An advantage SAM has over other traditional classifiers is the independence from intensity values permitting regions of shadow to also be classified accurately.

3.2.2 Support Vector machine (SVM) Classifier

SVM based classification is a well-recognized classification technique (Chutia et. al., 2014) where an N-1 dimensional hyperplane is used to separate the data by maximizing the margin between them. The hyperplane is called the optimal hyperplane and the data points closest to the hyperplane are the constraining factors and are called the support vectors (Suykens and Vandewalle, 1999). This suggests that SVM is a linear classifier. However, to account for non-linear classification, SVM can be used alongside kernels such as polynomial, RBF, sigmoid etc. (Sharma et. al., 2016). This study utilizes two commonly used kernels which have demonstrated significant success in the past (Gordon, 2004). The mathematical form of the polynomial kernel is given as below:

$$K(x, xi) = 1 + \sum_i (x * xi)^d \quad \text{... (5)}$$

Here, x is the input, xi is the support vector and d is the degree of the polynomial to be used. The RBF kernel expression is as follows:

$$K(x, xi) = e^{\left(-\Upsilon * (\sum_i (x - xi)^2)\right)} \quad \text{... (6)}$$

There are two parameters of concern that can be tweaked: the gamma parameter and the penalty parameter (Sharma et. al., 2016). The gamma parameter depicts the influence of the training sample with smaller values causing far reaching influence. The penalty parameter or the misclassification trade off parameter affects the smoothness of the decision boundary. Larger values cause over fitting.

3.2.3 Maximum Likelihood Classifier (MLC)

MLC is based on the Bayes law following posterior=prior*likelihood/evidence given by:

$$\mathrm{Lx} = \mathrm{P}\left(\frac{\omega}{\mathrm{x}}\right) = \frac{\mathrm{P}(\omega) * \mathrm{P}\left(\frac{\mathrm{x}}{\omega}\right)}{\mathrm{P}(\mathrm{x})} \quad \text{... (7)}$$

Generally, the prior probability of the for a class ω is assumed to be a constant or expected to be equal to each other and the evidence, P(x), is usually common to all classes, therefore L_x is dependent on P(x/ω). Classification is performed such that the likelihood of x belonging to a class ω is maximized (Strahler, 1980). Sampling should be such that the estimation of the mean and covariance is reflective of that of the population. The maximum likelihood method is not useful when the distribution of the population does not follow the normal distribution.

4. Results and discussion

For very small regions, we obtain better results using the higher spatial resolution images as expected. MLC consistently displayed best results with the RapidEye data due to the inferior performance of the classifier with higher number of bands (Houghes Phenomenon). For high inter class similarity, as is the case is for the water and vegetation classes in Test Site 2, we observe that the classification was performed best using the hyperspectral data of Hyperion and the Red Edge subset from the Hyperion data. Fused data is also observed to perform well in this case. For low interclass similarity in a small Test Site, however, we observe that fused data provides good results. However, the separability between the vegetated and non-vegetated classes is brought out better using the Red Edge subsets of the fused dataset and the Hyperion dataset. Thus the utility of the Red Edge subsetting for optimum feature extraction for classification is established. Details on the denoising, assessment of fusion and classification results are as documented in the following subsections.

4.1 Denoising Using the MNF Transform

The Eigen values and Eigen vectors of the image obtained are ordered (Figure 4). The image was then projected onto the Eigen space to decorrelate the bands and noise whitening was performed. The noise related Eigen values (normalized to 1) were discarded and the signal rich Eigen-images were employed for the inverse that generated us the denoised image that is used for classification.

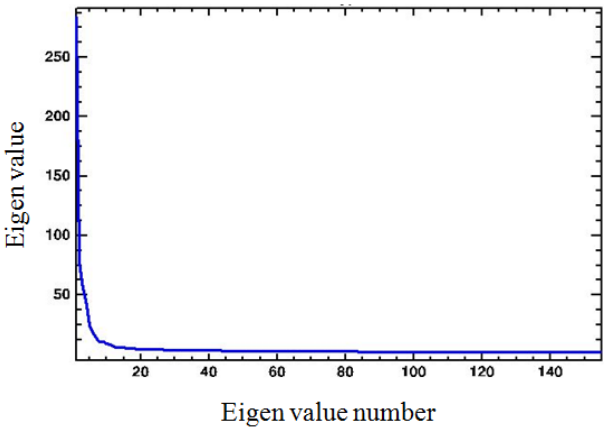

Figure 4: Eigen value graph based on which we select the Eigen values that can be used to maximize the SNR

4.2 Spectral characteristics of the fused product

From figure 5, we observe that the Gram Schmidt spectral sharpening leads to an offset in the intensity values of the fused product. In order to study if any distortion occurs or if the difference lies solely in the offset, we have performed a correlation test on the data set. Ten random regions were selected from both the Hyperion image and the fused image. The average spectrum of each region was computed and a scatter plot was used to check for the correlation. Very high correlation was observed with an average Pearson coefficient of correlation as 0.998 (Figure 6).

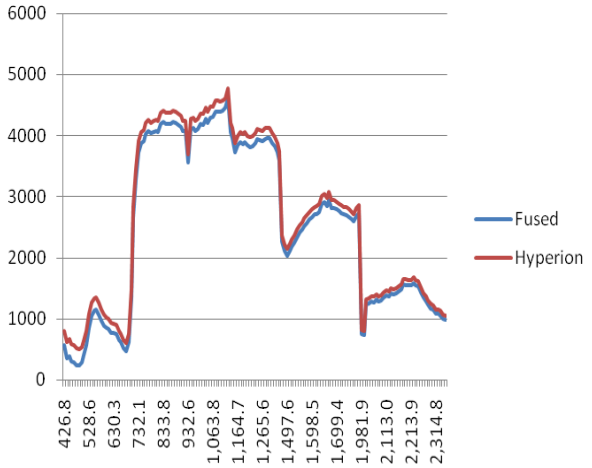

Figure 2: Spectrum of a vegetated region as displayed by the fused image and the Hyperion image after all corrections have been performed. X axis is wavelength in nm and y axis is reflectance.

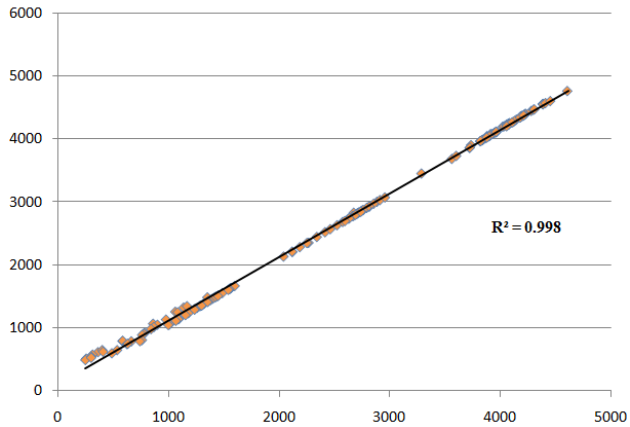

Figure 3: Scatter plot between fused spectra and Hyperion spectra

4.2 Classification results

The results of classification accuracy in the form of overall accuracy and kappa coefficients are documented in the tables 5-7.

Test site 1 classification yields a maximum accuracy by the Red Edge bands subset of the Hyperion image. However, the fused image and the Red Edge subset also depict similar high accuracy. The RapidEye image yields a maximum accuracy with the ML classifier, the fused image with the SVM classifier and the Hyperion image with the SVM classifier. The Red Edge spectral subsets of the fused and Hyperion image presented highest accuracies for the ML and the SVM classifiers respectively. The SVM classification results for each dataset for the test site is given in figure 6.

Test site two portrays a maximum accuracy for the RapidEye image with the ML classifier and the Hyperion image with the SVM classifier. The Red Edge spectral subset of the Hyperion also presents a comparable accuracy followed by the fused data set and the spectral subset of the same. The RapidEye image accuracies follow the order of ML, SVM and finally SAM classifiers. The Red Edge subset of Hyperion also follows the same order as expected. The Red Edge subset of the fused subset depicts a deviation from the expected results with SVM performing better than MLC in spite of the reduced number of bands. However, the Hyperion image and the fused image follow the expected trend of SVM accuracies greater than the SAM accuracies and finally the ML accuracies. This arises due to the Houghes phenomenon. The SVM classification results for each dataset for the test site is given in figure 7.

Test site 3 depicts maximum accuracies for the Hyperion image followed by the Red Edge subset of the Hyperion image. The RapidEye image and fused image classification results are also competitive. However, the Red Edge subset of the fused image displays a significantly deteriorated accuracy level. The performance of SVM is better in images with larger bands such as Hyperion and the fused product. SVM and ML classifiers perform comparably for the Red Edge subsets. However, the RapidEye image due to its minimum spectral bands and

high spatial resolution demonstrate a high accuracy with the ML classifier. ML classified output for Hyperion is not available due to lack of training samples. The SVM classification results for each dataset for the test site is given in figure 8.

Table 5: Table depicting overall accuracy and kappa coefficient for the RapidEye, Fused, Red Edge of Hyperion, Red Edge of Fused image and Hyperion images classified using the SAM, MLC, SVM with Polynomial order 3 and RBF kernel classifiers for Test Site 1

	SVM		SAM		MLC		SVM Poly	
	Kappa	Accuracy in %	Kappa	Accuracy in %	Kappa	Accuracy in %	Kappa	Accuracy in %
RapidEye	0.91	93.35	0.76	83.06	0.92	94.48	0.90	93.24
Fused	0.96	97.13	0.64	74.03	0.64	73.43	0.96	97.03
Red Edge Fused	0.93	95.16	0.70	78.28	0.95	96.57	0.93	95.02
Red Edge Hyperion	0.96	97.28	0.71	78.55	0.94	95.47	0.95	96.53
Hyperion	0.93	94.71	0.83	87.61	0.61	70.09	0.94	95.47

Table 6: Table depicting overall accuracy and kappa coefficient for the RapidEye, Fused, Red Edge of Hyperion, Red Edge of Fused image and Hyperion images classified using the SAM, MLC, SVM with Polynomial order 3 and RBF kernel classifiers for Test Site 2

	SVM		SAM		MLC		SVM Poly	
	Kappa	Accuracy in %	Kappa	Accuracy in %	Kappa	Accuracy in %	Kappa	Accuracy in %
RapidEye	0.84	87.51	0.76	81.21	0.87	89.86	0.84	87.48
Fused	0.79	83.30	0.54	64.19	0.53	61.43	0.78	82.99
Red Edge Fused	0.76	81.61	0.64	72.31	0.74	79.52	0.76	81.55
Red Edge Hyperion	0.85	88.24	0.60	68.34	0.87	89.61	0.85	87.99
Hyperion	0.87	89.23	0.81	84.61	0.41	51.56	0.86	88.99

Table 7: Table depicting overall accuracy and kappa coefficient for the RapidEye, Fused, Red Edge of Hyperion, Red Edge of Fused image and Hyperion images classified using the SAM, MLC, SVM with Polynomial order 3 and RBF kernel classifiers for Test Site 3

	SVM		SAM		MLC		SVM Poly	
	Kappa	Accuracy in %	Kappa	Accuracy in %	Kappa	Accuracy in %	Kappa	Accuracy in %
RapidEye	0.69	74.91	0.57	65.41	0.70	75.79	0.51	59.81
Fused	0.52	61.14	0.46	56.37	0.32	42.68	0.69	75.01
Red Edge Fused	0.51	60.37	0.45	56.33	0.51	60.05	0.51	60.10
Red Edge Hyperion	0.72	77.53	0.48	59.32	0.72	77.85	0.72	78.06
Hyperion	0.73	78.38	0.65	73.16	N/A	N/A	0.74	79.45

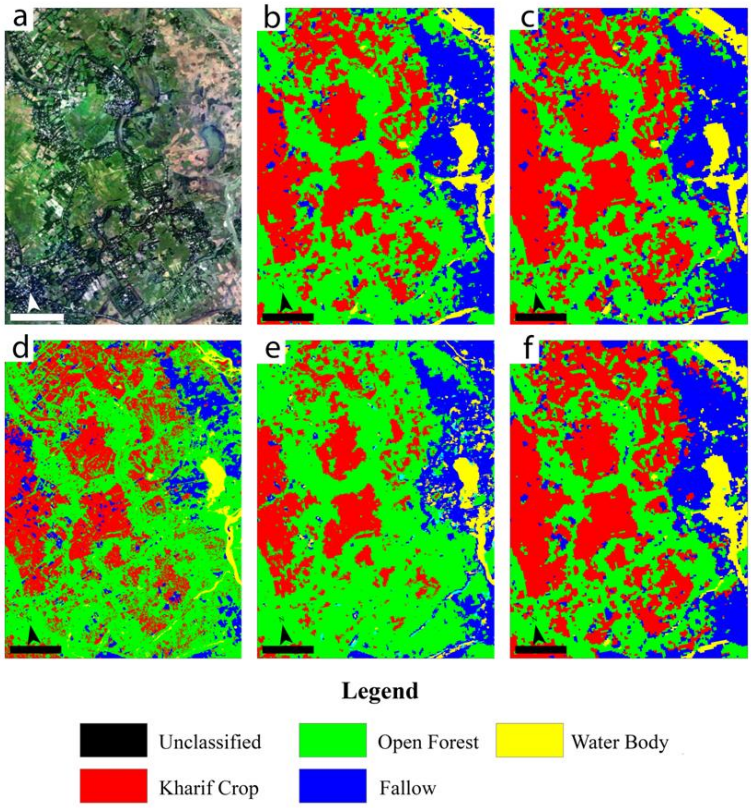

Figure 4: (a) RapidEye image as a reference, (b) the fused image classification results, (c) Hyperion image classification results, (d) RapidEye image classification results, (e) Red Edge subset of the fused image classification result and the (f) Red Edge subset of the Hyperion image classification result for Test Site 1

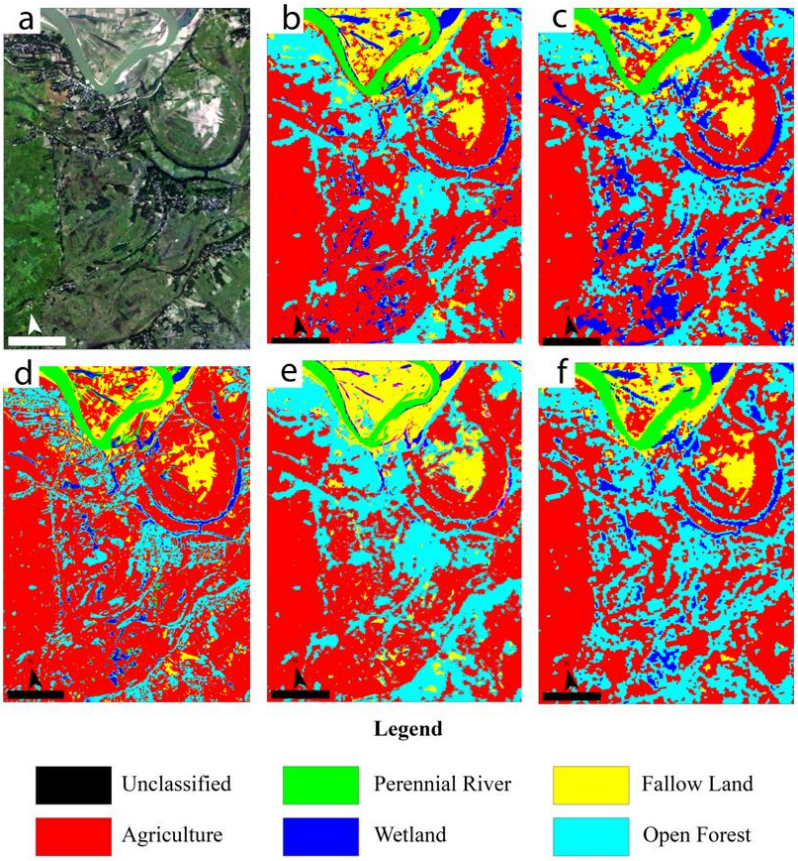

Figure 5: (a) RapidEye image as a reference, (b) the fused image classification results, (c) Hyperion image classification results, (d) RapidEye image classification results, (e) Red Edge subset of the fused image classification result and the (f) Red Edge subset of the Hyperion image classification result for Test Site 2

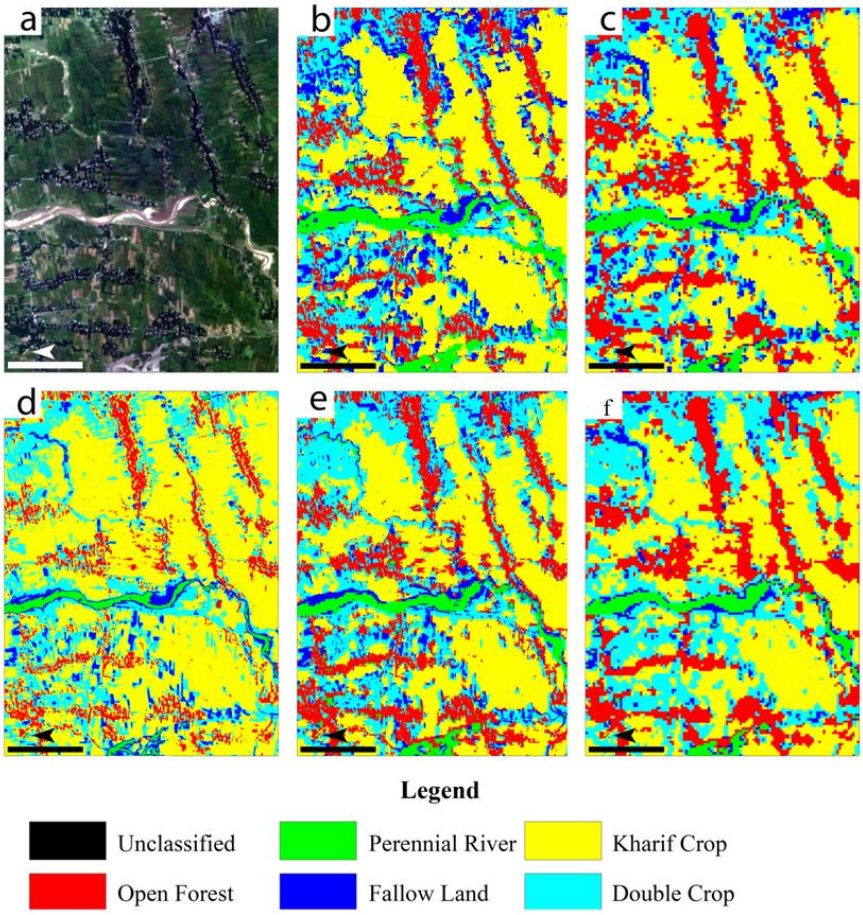

Figure 6: (a) RapidEye image as a reference, (b) the fused image classification results, (c) Hyperion image classification results, (d) RapidEye image classification results, (e) Red Edge subset of the fused image classification result and the (f) Red Edge subset of the Hyperion image classification result for Test Site 3

5. Conclusion

Satellite images permit accurate mapping of the land cover via high spatial resolution multispectral images such as those of RapidEye, CartoSat, SkySat, PlanetScope, WorldView series etc. However, to distinguish within the more similar land use features, spectral identification is required. The use of hyperspectral imagery thus provides additional spectral features for use in the various classification techniques. However, due to the low spatial resolution of hyperspectral imagery, the fused products were generated and their utilities tested with established classification techniques. Our results suggest optimal classifiers to be used with the types of data are independent of the test site and depend only upon the sensor and number of bands. RapidEye data classifies the scene best with the MLC classifier. However, as the number of bands increases as is the case with the fused or Hyperion images, MLC responds in a sub-optimal manner. SVM classifiers with RBF or polynomial kernels perform consistently better. Red Edge subsets of the Hyperion and fused images are observed to perform well with both MLC and SVM classifiers. With regard to the Test Sites, RapidEye images can be directly used for classification in case of diverse and less number of classes. Hyperion data can be used where there exists similarity within the data such as multiple vegetation classes where minute differences in the spectra come into consideration. However, best results are observed with the red edge subsets of the fused and Hyperion data sets. In case of small regions approaching the fused red edge subset performs better. However, if the spatial resolution of the Hyperion data is not limiting, it presents comparable results.

The fusion technique in this study exhibited good results in smaller regions where resolution of land cover classes at proximity are required. However, on larger scales, the results are obsolete when compared to hyperspectral image classification. This however can be improved by usage of other fusion techniques (Yokoya et. al., 2017, Akhtar et. al., 2015). An aspect to be considered for future applications include the utilization of high spatial resolution multispectral data via Unmanned Aerial Vehicles (UAV) or aircrafts with low resolution satellite based hyperspectral data for accurate cm level mapping and classification of the land use.

Acknowledgements

The authors would like to thank the facilities provided by North Eastern Space Applications Centre (NESAC), Department of Space, Government of India, Shillong, Meghalaya, India for providing the satellite datasets and the necessary scientific tools and environment to accomplished this work.

References

Akhtar, N., F. Shafait and A. Mian (2015). Bayesian sparse representation for hyperspectral image super resolution, In Proceedings of the IEEE Conference on Computer Vision and Pattern Recognition, 3631-3640.

Bernstein, L. S., Adler-Golden S. M., Sundberg R. L., Levine R.Y, Perkins T.C., Berk A., Ratkowski A.J., Felde G., Hoke M.L.., (2005). Validation of the QUick Atmospheric Correction (QUAC) algorithm for VNIR-SWIR multi- and hyperspectral imagery. SPIE Proceedings, Algorithms and Technologies for Multispectral, Hyperspectral, and Ultraspectral Imagery XI, 5806, 668-678.

Breunig, F.M., L.S. Galvao, A.R. Formaggio and J.C. Epiphanio (2011). Classification of soybean varieties using different techniques: case study with Hyperion and sensor spectral resolution simulations, Journal of Applied Remote Sensing, 5(1), 053533-053533.

Ceccato, P, Flasse S, Tarantola S, Jacquemond S, Gregoire J.M. (2001). Detecting vegetation leaf water content using reflectance in the optical domain. Remote Sensing of Environment, 77(1), 22-33

Champagne, C. M., Staenz K, Bannari A, McNairn H, DeGuise J.C. (2003). Validation of a hyperspectral curve-fitting model for the estimation of plant water content of agricultural canopies. Remote Sensing of Environment 87(2-3) , 148-160.

Cho, M. A., Sobhan, I., Skidmore, A. K., & De Leeuw, J. (2008). Discriminating species using hyperspectral indices at leaf and canopy scales. The International Archives of the Photogrammetry, Remote Sensing and Spatial Information Sciences, 37(B7), 369-376.

Chutia, D. and D.K. Bhattacharyya (2010). An efficient approach for extraction of linear features from high resolution Indian satellite imageries, PAN, 12000, 1223-1227.

Chutia, D., D.K. Bhattacharyya, K.K. Sarma, R. Kalita, and S. Sudhakar (2015). Hyperspectral remote sensing classifications: a perspective survey. Transactions in GIS, 20(4), 463-490.

Chutia, D., D.K. Bhattacharyya, R. Kalita and S. Sudhakar (2014). OBCsvmFS: Object-based classification supported by support vector machine feature selection approach for hyperspectral data Journal of Geomatics, 8(1), 12-19.

Daughtry, C. S., Doraiswamy, P. C., Hunt Jr, E. R., Stern, A. J., McMurtrey Iii, J. E., & Prueger, J. H. (2006). Remote sensing of crop residue cover and soil tillage intensity. Soil and Tillage Research, 91(1-2), 101-108.

Ferrato, L.J. and K.W. Forsythe (2012). Comparing hyperspectral and multispectral imagery for land classification of the lower Don river. Toronto, Journal of Geography and Geology, 5(1), 92-107.

Gao, B.C. (1996). NDWIA normalized difference water index for remote sensing of vegetation liquid water from space, Remote Sensing of Environment, 58.3, 257-266

Green, A.A., M.D. Craig, and C. Shi (1988). The application of the minimum noise fraction transform to the compression and cleaning of hyper-spectral remote sensing data, Geoscience and Remote Sensing Symposium, IGARSS'88, Remote Sensing: Moving Toward the 21st Century, International, 3, 1807-1807

Gupta, R.K., D. Vijayan and T.S. Prasad (2003). Comparative analysis of red-edge hyperspectral indices. Advances in Space Research, 32(11), 2217-2222.

Heiden, U., W. Heldens, S. Roessner, K. Segl,T. Esch, and A. Mueller (2012). Urban structure type characterization using hyperspectral remote sensing and height information, Landscape and urban Planning, 105(4), 361-375.

Jackson, R.D. and A.R. Huete (1991). Interpreting vegetation indices. Preventive veterinary medicine, 11(3-4), 185-200.

Jensen, J.R. and J. Im, (2007). Remote sensing change detection in urban environments, Geo-spatial technologies in urban environments, Springer Berlin Heidelberg, 7-31.

Laben, C.A. and B.V. Brower (2000) Eastman Kodak Company, Process for enhancing the spatial resolution of multispectral imagery using pan-sharpening, U.S. Patent 6,011,875.

Lang, M. F. Stober and H.K. Lichtenthaler (1991) Fluorescence emission spectra of plant leaves and plant constituents, Radiat Environ Biophys 30(4), 333-347.

Maurer, T. (2013). How to pan-sharpen images using the Gram-Schmidt pan-sharpen method-a recipe. International Archives of the Photogrammetry, Remote Sensing and Spatial Information Sciences, 1, 239-244.

Pearlman, J., P. Barry, C. Segal, J. Shepanski, D. Beiso, S. Carman (2003). Hyperion, a Space Based Imaging Spectrometer, IEEE Transactions on Geoscience and Remote Sensing, 41(6), 1160-1173.

Penuelas, J., F. Baret, and I. Filella. (1995) Semi-empirical indices to assess carotenoids chlorophyll a ratio from leaf spectral reflectance, Photosynthetica 31.2, 221-230.

Pignatti, S., R.M. Cavalli, V. Cuomo, L. Fusilli, S. Pascucci, M. Poscolieri, and F. Santini (2009). Evaluating Hyperion capability for land cover mapping in a fragmented ecosystem: Pollino National Park, Italy, Remote Sensing of Environment, 113(3), 622-634.

Pohl, C (2013). Challenges of Remote Sensing Image Fusion to Optimize Earth Observation Data Exploitation, European Scientific Journal, 4, 355-365

Porra R.J, Thomson W.A, Kriedemann P.E, (1989). Determination of accurate extinction coefficients and simultaneous equations for assaying chlorophylls a and b

extracted with four different solvents: verification of the concentration of chlorophyll standards by atomic absorption spectroscopy, Biochimica et Biophysica Acta (BBA) - Bioenergetics, 975(3), 384-394,

Purkis, S. J., and V.V. Klemas (2011). Remote Sensing and Global Environmental Change, Wiley-Blackwell ltd., 1-367

Schuster, C., M. Förster and B. Kleinschmit (2012). Testing the Red Edge channel for improving land-use classifications based on high-resolution multi-spectral satellite data, International Journal of Remote Sensing, 33(17), 5583-5599.

Serrano, L., J. Penuelas J, and Ustin S.L. (2002). Remote sensing of nitrogen and lignin in Mediterranean vegetation from AVIRIS data: Decomposing biochemical from structural signals, Remote Sensing of Environment, 81(2-3), 255-264

Sharma, V., D. Baruah, D. Chutia, P.L.N. Raju and D.K. Bhattacharya (2016). An assessment of support vector machine kernel parameters using remotely sensed satellite data, In Recent Trends in Electronics, Information & Communication Technology (RTEICT), 1567-1570.

Smith, K.L., M.D. Steven, and J.J. Colls (2004). Use of hyperspectral derivative ratios in the red-edge region to identify plant stress responses to gas leaks, Remote sensing of environment, 92(2), 207-217.

Stimson, H. C., Breshears, D. D., Ustin, S. L., & Kefauver, S. C. (2005). Spectral sensing of foliar water conditions in two co-occurring conifer species: Pinus edulis and Juniperus monosperma. Remote Sensing of Environment, 96(1), 108-118.

Strahler, A. H. (1980). The use of prior probabilities in maximum likelihood classification of remotely sensed data, Remote Sensing of Environment, 10(2), 135-163.

Suykens, J. A., & J. Vandewalle (1999). LEast squares support vector machine classifiers. Neural processing letters, 9(3), 293-300.

Ustuner, M., F.B. Sanli and B. Dixon (2015). Application of support vector machines for landuse classification using high-resolution RapidEye images: a sensitivity analysis, European Journal of Remote Sensing, 48(1), 403-422.

Vogelmann, T.C. (1993). Plant tissue optics, Annual review of plant biology, 44(1), 231-251

Wu, C., Niu, Z., Tang, Q., & Huang, W. (2008). Estimating chlorophyll content from hyperspectral vegetation indices: Modeling and validation. Agricultural and forest meteorology, 148(8-9), 1230-1241.

Yokoya, N., C Grohnfeldt and J Chanussot (2017). Hyperspectral and Multispectral Data Fusion: A Comparative Review, IEEE Geoscience and Remote Sensing Magazine, 1-25

Yuhas, R. H., A.F. Goetz and J.W. Boardman (1992). Discrimination among semi-arid landscape endmembers using the spectral angle mapper (SAM) algorithm. JPL, Summaries of the Third Annual JPL Airborne Geoscience Workshop. Volume 1: AVIRIS Workshop,147-149.